Flow Turbulence Combust
DOI 10.1007/s10494-013-9523-3

Structural Wall-modeled LES Using a High-order Spectral Difference Scheme for Unstructured Meshes

Guido Lodato · Patrice Castonguay · Antony Jameson

Received: 15 December 2012 / Accepted: 30 October 2013

Abstract The combination of the high-order unstructured Spectral Difference (SD) spatial discretization scheme with Sub-Grid Scale (SGS) modeling for Wall-Modeled Large-Eddy Simulation (WMLES) is investigated. Particular focus is given to the use of wall-function approaches and to the relevant optimal coupling with the numerical scheme and the SGS model, a similarity mixed type model featuring newly designed discrete filters with specified cutoff length scale. To take full advantage of the discontinuous Finite Element (FE) structure which characterizes the SD scheme, wall-modeling is accomplished within the first wall element by using the information from the farthest solution points from the wall. Compared to the customary used first off-wall node, this point provides more accurate information to the wall-function, thus improving the quality of the solution. Two different wall-models are tested, a classical three-layers wall-function based on the equilibrium assumption and a more general formulation to account for the pressure gradient in more complex configurations. Moreover, the mixed scale-similarity SGS model is used in the entire computational domain without any particular adjustment inside the wall-modeled region. Numerical tests on the classical test case of the turbulent channel flow at different Reynolds numbers and on the channel with periodic constrictions at $Re_h = 10{,}595$ give evidence that the results are extremely sensitive to the choice of the solution points used to provide the informations to the law-of-the-wall. In particular, it is shown that significant improvements in the results can be attained by solving the wall-function away from the wall, rather than at the first off-wall solution point as customary done. The combination of the selected wall-modeling strategies and the similarity mixed formulation proves to be remarkably accurate, even in the presence of boundary layer separation, thus opening the path to further exploit the high-order SD platform, as well as a broad range of other similar methodologies, for WMLES. Extensions of the methodology are envisaged to include more

G. Lodato (✉)
INSA de Rouen - CORIA, Energy & Propulsion, 76801 St. Etienne du Rouvray, France
e-mail: guido.lodato@insa-rouen.fr

G. Lodato · P. Castonguay · A. Jameson
Stanford University, Aeronautics & Astronautics, Stanford, CA 94305-4035, USA

Published online: 17 November 2013

sophisticated wall-modeling approaches incorporating turbulent sensors to switch to no-slip conditions in laminar regions.

Keywords High-order schemes · Unstructured meshes · Large-Eddy simulation · Similarity mixed models · Wall-modeling

1 Introduction

In a large number of LES applications the underlying numerical platform consists of highly dissipative and at most second-order schemes. The inherent numerical dissipation introduced by such numerical schemes can limit their ability to represent the spectrum resolved in LES. Although the increasing availability in computational power can, in some cases, allow some flexibility in reducing numerical error and dissipation by increasing grid resolution, there are still many flow problems (e.g., vortex dominated flows) for which the use of low-order methods would be too expensive, unsuitable or even impractical [60]. For such flows, high-order methods represent a more viable option. Undoubtably, the continuous improvements toward the development of robust and reliable high-order schemes for DNS and LES, and the relevant capabilities in representing the flow and the underlying physics with increasing levels of detail, have made it possible to tackle hitherto intractable problems in fundamental research. Therefore, the combination of high-order numerical schemes with advanced SGS modeling techniques seems a very attractive option to make LES a valuable and reliable tool for high-fidelity computations for fundamental flow physics and industrial applications. Unfortunately, many available high-order numerical schemes are designed to be used on cartesian or very smooth structured curvilinear meshes and are inadequate to simulate turbulent flows over complex geometries. In the current work, the optimal coupling between a high-order solver for unstructured hexahedral meshes, an explicit filtering LES method and Reynolds-Averaged Navier-Stokes (RANS) type wall-function approaches is investigated. The resulting tool allows to perform highly accurate turbulent flow computations over realistic geometries.

High-order numerical schemes for solving the compressible Navier-Stokes equations on unstructured grids have been widely studied during the last decade. By far the most mature and widely used of these schemes are based on the Discontinuous Galerkin (DG) method [16, 23]. Recently, however, several alternative high-order methods have been proposed, including SD type schemes [19, 20, 27, 32, 34, 54], which potentially offer increased efficiency compared with DG methods. A recent study addressed the implementation of the WALE Similarity Mixed (WSM) model [35] into the SD spatial discretization for 3D unstructured hexahedral grids [36]. As a result, two distinct classes of discrete filtering operator satisfying selected criteria in terms of cutoff and locality were developed and tested on the turbulent channel flow at different Reynolds number using both Cartesian and unstructured meshes. This numerical platform for high-order explicit LES represents the base of the present work, which is aimed at extending the code capabilities to allow wall-modeled LES. It is worthwhile stressing that the assessment and the comparison of different SGS modeling formulations are outside the scope of the present study, whose main subject is the development and validation of an optimal strategy to incorporate wall-modeling into the SD scheme.

In fact, although the combination of the high-order SD method with a suitable implementation of a scale similarity SGS model has proven to be an extremely promising tool, the

Reynolds number scaling of the necessary number of Degrees of Freedom (DoF) for wall-resolved LES (WRLES) still limits significantly the applicability of LES to wall bounded turbulent flows of practical engineering interest [9, 10]. Aside from considerations about the number of DoF, when explicit time integration is performed, the scales involved in the boundary layer and the relevant grid resolution can constrain the time-step via the CFL limitation such as to make it practically impossible to get reasonably converged results and/or statistics within an acceptable time. For LES to become a viable option in a broad range of applications, reliable and accurate wall-modeling approaches are needed.

An interesting approach in the direction of making LES more *engineering-friendly* involves the simultaneous use of RANS and LES (*cf.* Refs. [44, 45] for a review of typical approaches). The idea is to use LES to solve the unsteady features of interest while leaving to RANS the burden of solving prohibitively small features which might not be of direct interest, such as boundary layers. The most simple approach is to couple the LES solution with wall-functions based on the equilibrium-stress hypothesis. A comparison of different combinations of wall-functions and SGS modeling strategies can be found in Ref. [55]. One limit in the applicability of these rather simple techniques is the availability of sufficiently general wall-functions, in particular when the equilibrium-stress hypothesis does not hold true. To overcome such limitations, more sophisticated wall-functions have been developed to reproduce non-equilibrium turbulent boundary layers subject to favorable or adverse pressure gradients [7, 12] or to account for compressibility effects [3]. Other more general approaches involve, for instance, the solution of the (1D Reynolds-averaged) turbulent boundary-layer equations in the inner layer using information (*viz.* boundary conditions) from the LES in the outer layer [2, 4, 8, 25, 59].

Even if finding an appropriate way to blend the RANS model in the inner layer and the LES model in the outer layer remains an extremely delicate point, recent studies [24, 29, 42] have suggested that, despite the simplicity of wall-modeling procedures and zonal techniques, extremely accurate results can be still obtained by properly addressing the numerical implementation of the model, rather than the model itself. Inspired by this observation and leveraging on the particularly convenient structure of the SD scheme which, thanks to the FE discretization of the solution, represents an ideal numerical platform to develop wall-modeling approaches based on wall-functions or embedded RANS layers, the main subject of the present study is the development of an optimal strategy to couple the SGS model with the law-of-the-wall.

In particular, recognizing that wall elements can be easily designed to model the inner layer with the required accuracy without major implementation difficulties (for instance, in terms of code parallelism), two different RANS type wall-functions are directly coupled with the WSM model. Numerical tests on the classical channel flow, as well as, on a channel with periodic constrictions involving flow separation and reattachment, show that, despite the simplicity of the proposed approach, a suitable choice for the way the SGS model and the wall-function are interlinked can lead to significant improvements in the results. The method can be generalized to include more advanced wall-modeling formulations, and extended in a straightforward way to a broad range of discontinuous FE type schemes, including DG methods and the whole class of recently developed energy stable Flux Reconstruction schemes [22, 56, 57, 61].

2 Mathematical Formulation

2.1 The numerical scheme

The Navier-Stokes equations are solved using the high-order SD method for unstructured spatial discretization. The formulation of the equations on hexahedral grids is similar to the formulation by Sun et al. [54], which will be summarized below for completeness. After introducing the *bar* filter operator and the density-weighted Favre filter operator *tilde*, the unsteady compressible Navier-Stokes equations in conservative form are written as

$$\frac{\partial \overline{\boldsymbol{U}}}{\partial t} + \frac{\partial \overline{\boldsymbol{F}}^k}{\partial x_k} = \boldsymbol{0}, \tag{1}$$

where $\overline{\boldsymbol{U}} = \left(\overline{\rho}\ \overline{\rho u_1}\ \overline{\rho u_2}\ \overline{\rho u_3}\ \overline{\rho e}\right)^{\mathrm{T}}$ is the vector of conservative variables, and $\overline{\boldsymbol{F}}^k = \overline{\boldsymbol{F_I}}^k - \overline{\boldsymbol{D}}^k$ accounts for the inviscid and viscous flux vectors

$$\overline{\boldsymbol{F_I}}^k = \begin{pmatrix} \overline{\rho u}_k \\ \overline{\rho u}_1 \widetilde{u}_k + \delta_{1k}\overline{\varpi} \\ \overline{\rho u}_2 \widetilde{u}_k + \delta_{2k}\overline{\varpi} \\ \overline{\rho u}_3 \widetilde{u}_k + \delta_{3k}\overline{\varpi} \\ (\overline{\rho e} + \overline{\varpi})\widetilde{u}_k \end{pmatrix}, \qquad \overline{\boldsymbol{D}}^k = \begin{pmatrix} 0 \\ 2\overline{\mu}\widetilde{A}_{1k} + \tau^{\mathrm{d}}_{1k} \\ 2\overline{\mu}\widetilde{A}_{2k} + \tau^{\mathrm{d}}_{2k} \\ 2\overline{\mu}\widetilde{A}_{3k} + \tau^{\mathrm{d}}_{3k} \\ 2\overline{\mu u}_j \widetilde{A}_{kj} + \frac{\overline{\mu} c_p}{Pr}\frac{\partial \widetilde{\vartheta}}{\partial x_k} + q_k \end{pmatrix}. \tag{2}$$

In the above equations, ρ is the fluid's density, u_k is the velocity vector, e is the total energy (internal + kinetic), μ is the dynamic viscosity, A_{ij} is the deviator of the deformation tensor, c_p is the specific heat capacity at constant pressure and Pr is the Prandtl number. Furthermore, $\overline{\varpi}$ and $\widetilde{\vartheta}$ are the filtered *macro-pressure* and *macro-temperature* [31, 35], these quantities being related by the usual equation of state

$$\overline{\varpi} = \overline{\rho} R \widetilde{\vartheta}, \quad \text{and} \quad \overline{\rho e} = \frac{\overline{\varpi}}{\gamma - 1} + \frac{1}{2}\overline{\rho u}_k \widetilde{u}_k, \tag{3}$$

where R represents the gas constant and $\gamma = c_p/c_v$ is the ratio between specific heat capacities at constant pressure and volume. The unclosed SGS terms in the momentum and energy equations are indicated in Eq. (2) as τ_{ij} and q_k, respectively (note that the superscript 'd' refers to the deviatoric part of the relevant tensor).

To achieve an efficient implementation, all elements in the physical domain are transformed to a standard cubic element described by local coordinates $\boldsymbol{\xi} = (\xi_1, \xi_2, \xi_3)$, with $\boldsymbol{\xi} \in [0:1]^3$. The governing equations in the physical domain are then transferred into the computational domain, and they take the form

$$\frac{\partial \overline{\boldsymbol{\mathcal{U}}}}{\partial t} + \frac{\partial \overline{\boldsymbol{\mathcal{F}}}^k}{\partial \xi_k} = \boldsymbol{0}, \tag{4}$$

where

$$\overline{\boldsymbol{\mathcal{U}}} = |\det(\mathsf{J})|\overline{\boldsymbol{U}}, \quad \overline{\boldsymbol{\mathcal{F}}}^k = |\det(\mathsf{J})|\frac{\partial \xi_k}{\partial x_j}\overline{\boldsymbol{F}}^j, \tag{5}$$

and $\det(\mathsf{J})$ represents the determinant of the Jacobian matrix $\mathsf{J}_{ij} = \partial x_i/\partial \xi_j$.

Within each standard element, two sets of points are defined, namely the solution points and the flux points, as schematically illustrated in Fig. 1 for a one-dimensional element. In order to construct a degree $(N-1)$ polynomial for each coordinate direction, solution at N points are required. These N points in 1D are chosen to be the Gauss-Legendre quadrature points, whereas the flux points are selected to be the Gauss-Legendre quadrature points of

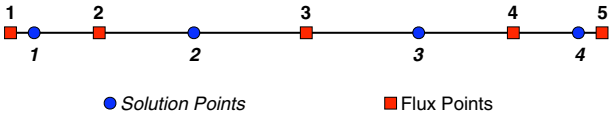

Fig. 1 Schematic representation of the one dimensional distribution of solution and flux points within the SD element for $N = 4$

order $N - 1$ plus the two end points 0 and 1. This particular combination of solution and flux points, in fact, can be proved to be linearly stable for all orders of accuracy and optimal in reducing aliasing errors and providing good conditioning for the non-linear case [21, 22]. Using the N solution points and the $N + 1$ flux points, polynomials of degree $N - 1$ and N, respectively, can be built using Lagrange bases defined as

$$h_i(\xi) = \prod_{s=1, s\neq i}^{N} \left(\frac{\xi - \xi_s}{\xi_i - \xi_s} \right), \quad \text{and} \quad l_{i+1/2}(\xi) = \prod_{s=0, s\neq i}^{N} \left(\frac{\xi - \xi_{s+1/2}}{\xi_{i+1/2} - \xi_{s+1/2}} \right). \tag{6}$$

The reconstructed solution for the conserved variables in the standard element is then obtained as the tensor product of the three one-dimensional polynomials,

$$\overline{\boldsymbol{U}}(\boldsymbol{\xi}) = \sum_{k=1}^{N} \sum_{j=1}^{N} \sum_{i=1}^{N} \frac{\overline{\boldsymbol{U}}_{i,j,k}}{|J_{i,j,k}|} h_i(\xi_1) h_j(\xi_2) h_k(\xi_3), \tag{7}$$

where i, j and k are the indices of the solution points within each standard element. A similar reconstruction is adopted for the resolved fluxes $\overline{\boldsymbol{\mathcal{F}}}^k$.

The reconstructed fluxes are only element-wise continuous, but discontinuous across cell interfaces. For the inviscid flux, a Riemann solver is employed to compute a common flux at cell interfaces to ensure conservation and stability. In the current implementation, the Roe solver with entropy fix [15, 47] is used. The left and right states here represent the solution on both sides of the shared edge flux point. The viscous flux is a function of both the conserved variables and their gradients, therefore, the solution gradients have to be calculated at the flux points. The average approach described by Sun et al. [54] is used to compute the viscous fluxes at the elements' interfaces.

2.2 LES modeling approach

To close the SGS terms in Eq. (2), the WSM model proposed by Lodato et al. [35] is here adopted. This model, in particular provides all the advantages of similarity formulations [13, 17, 33, 50] while ensuring correct near-wall scaling without the expense of dynamic procedures and stabilization averaging steps. The SGS stress tensor and heat flux are modeled as

$$\tau_{ij}^{\mathrm{d}} = 2\overline{\rho}\nu_{\mathrm{sgs}}\widetilde{A}_{ij} - \overline{\rho}\left(\widehat{\widetilde{u}_i\widetilde{u}_j} - \widehat{\widetilde{u}}_i\widehat{\widetilde{u}}_j\right)^{\mathrm{d}}, \tag{8}$$

$$q_k = \gamma\overline{\rho}\kappa_{\mathrm{sgs}}\frac{\partial\widetilde{e_I}}{\partial x_k} - \gamma\overline{\rho}\left(\widehat{\widetilde{e_I}\widetilde{u}_k} - \widehat{\widetilde{e}}_I\widehat{\widetilde{u}}_k\right), \tag{9}$$

where $\widetilde{e_I}$ is the resolved internal energy and the *hat* operator represents filtering at cutoff length $\alpha\Delta_{\mathrm{g}}$, where Δ_{g} is a measure of the actual grid resolution (see Eq. (11) below), and $\alpha \geq 1$ [33]. In the present study, newly developed constrained discrete filters for FE type

schemes are adopted [36]. In particular, discrete filters by Gauss quadrature integration are here used with cutoff length $1.5\Delta_g$ (*cf.* Section 2.4). The SGS kinematic viscosity, ν_{sgs}, and thermal diffusivity, κ_{sgs}, are computed as [41]

$$\nu_{sgs} = C_w^2 \Delta_g^2 \frac{\left(\widetilde{s}_{ij}^d \widetilde{s}_{ij}^d\right)^{3/2}}{\left(\widetilde{A}_{ij}\widetilde{A}_{ij}\right)^{5/2} + \left(\widetilde{s}_{ij}^d \widetilde{s}_{ij}^d\right)^{5/4}}, \quad \text{and} \quad \kappa_{sgs} = \frac{\nu_{sgs}}{Pr_{sgs}}, \tag{10}$$

where $C_w = 0.5$, and $\widetilde{s}_{ij}^d$ is the traceless symmetric part of the square of the resolved velocity gradient tensor $\widetilde{g}_{ij} = \partial \widetilde{u}_i / \partial x_j$. The sub-grid scale Prandtl number, Pr_{sgs}, is assumed constant and equal to 0.5 [13, 53], and Δ_g is computed from its counterpart in computational space, namely $\Delta = 1/N$, as [43]

$$\Delta(\boldsymbol{\xi}) \sim \left[\frac{|\det(\mathrm{J}(\boldsymbol{\xi}))|}{N^3}\right]^{1/3} = \Delta |\det(\mathrm{J}(\boldsymbol{\xi}))|^{1/3}. \tag{11}$$

2.3 Wall-modeling approach

Assuming that the streamwise and wall-normal directions are x_1 and x_2, respectively, a generic wall-function can be written as

$$\widetilde{u}_1^* = f_{LW}(x_2^*), \tag{12}$$

where $\widetilde{u}_1^*$ and x_2^* represent the normalized (filtered) velocity and the distance from the wall, respectively. Note that the normalization parameters are both a function of the wall shear stress τ_w. Eq. (12) shall be solved inside each wall element in order to obtain the wall shear stress to be imposed as a boundary condition at the wall. A schematic representation of the proposed wall-modeling strategy is depicted in Fig. 2. In particular, the wall shear stress is evaluated using information (e.g. wall distance and velocity magnitude in the plane tangential to the wall) from the farthest solution points from the wall (hereafter referred to

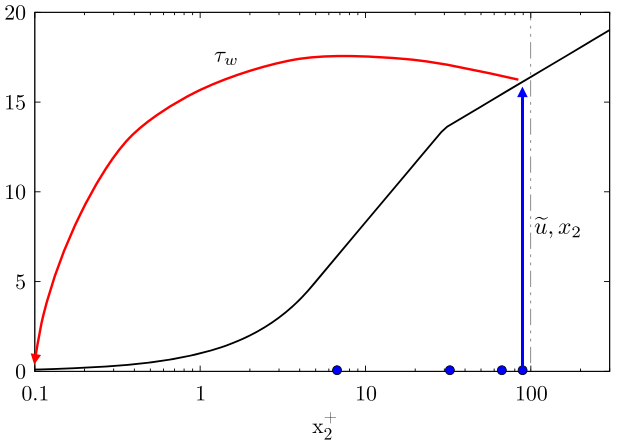

Fig. 2 Schematic representation of the wall-modeling strategy within a wall element ($N = 4$). *Blue dots* represent actual solution points in logarithmic scale; *colored arrows* represent the flow of information from the wall-farthest point to the wall-function and down to the wall

as sampling point). This particular point is used because the relevant information is more accurate than the other more under resolved points closer to the wall [24, 29]. Note that, as it will become evident looking at the results presented in Section 3.1.2, these points serve mostly as a support for the solution within the wall modeled region. The absence of direct coupling between the viscous flux at the wall and the solution (and its gradients) in the vicinity of the wall-closest point cannot ensure that a physically relevant flow be established through these points, which shall hence be disregarded when analyzing results. Tests conducted using the more commonly used first off-wall solution (or grid) point fully confirm that sampling too close to the wall can lead to a significant deterioration of the solution accuracy (*cf.* Section 3).

This is a crucial step in the procedure. In fact, even if using Reynolds-averaged information (e.g., from a law-of-the-wall, as in the present case, or the local integration of 1D turbulent boundary-layer equations) on an instantaneous unsteady flow from LES can be questionable from the theoretical point of view, the overall effect can be considered analogous to the application of relaxed boundary conditions: the instantaneous solution is characterized by the chaotic pattern of the resolved large-scale structures, but its long time average tends to be consistent with what is imposed as a boundary condition (e.g. the average wall shear stress). The outcome of the approach is clearly strongly influenced by the accuracy of this (relaxed) boundary condition, which in turn, is determined by the quality of the information at the sampling points and the accuracy of the wall-function.

Regarding the LES model used within the outer layer, this is applied unchanged throughout the wall-modeled region, the only exception being that the viscous flux at the wall is completely overridden by the one computed using the wall-function.

Two different wall-functions have been tested in the present work, namely, the classical three-layers wall-function by Breuer and Rodi [6] for zero pressure gradient turbulent boundary layers, and the more sophisticated wall-function proposed by Duprat et al. [12] for non-equilibrium turbulent boundary layers subject to favorable or adverse pressure gradients. These approaches are detailed in the two sections that follow.

2.3.1 Equilibrium wall-function approach

In the case of equilibrium boundary layers, Eq. (12) can be conveniently written as a three-layers wall-function [6] (hereafter referred to as BR) in the form

$$\widetilde{u}_1^+ = \begin{cases} x_2^+ & \text{if } x_2^+ \leq 5, \\ A \ln\left(x_2^+\right) + B & \text{if } 5 < x_2^+ \leq 30, \\ \kappa^{-1} \ln\left(E x_2^+\right) & \text{if } x_2^+ > 30, \end{cases} \tag{13}$$

with $\kappa = 0.42$ the von Kármán constant, $E = 9.8$, $A = [\kappa^{-1} \ln(30E) - 5]/\ln(6)$ and $B = 5 - A \ln(5)$. In this particular case, the '+' superscript is used to denote the classical scaling using the friction velocity $u_\tau = \sqrt{|\tau_w|/\rho_w}$ and the viscous length $\ell_\tau = \nu/u_\tau$, respectively (note that the subscript w is hereafter adopted to indicate quantities evaluated at the wall).

Except where explicitly set forth differently, to avoid the iterative inversion of the log-law (x_2^+ is itself a function of the unknown τ_w), the normalized wall distance x_2^+ is first computed using the shear stress from the previous time-step, as suggested by Wang and Moin [59]. Once the right-hand-side of Eq. (13) is computed, the wall shear stress is

obtained from the definition of $\widetilde{u}_1^+$ and the instantaneous value of the velocity. The simplifying assumption is made that the instantaneous wall shear stress is in phase and aligned with the velocity at the sampling location.

With regards to the energy equation, a two-layers wall-function is used to compute the wall heat flux q_w [51]:

$$\frac{q_w u_\tau}{\gamma \tau_w} = \begin{cases} (\widetilde{e_I} - e_w)(\widetilde{u}_1^+ Pr)^{-1} & \text{if } x_2^+ \leq 11.8, \\ (\widetilde{e_I} - e_w)[(\widetilde{u}_1^+ + C)Pr_t]^{-1} & \text{if } x_2^+ > 11.8, \end{cases} \tag{14}$$

where $\widetilde{e_I}$ is the internal energy at the sampling point, $e_w = c_v \vartheta_w$ accounts for the imposed wall temperature, $Pr_t = 0.9$ is the turbulent Prandtl number, and $C = 11.8 \times (Pr/Pr_t - 1)$ from the matching condition at $x_2^+ = 11.8$.

2.3.2 Non-equilibrium wall-function approach

To overcome the limitations brought by the equilibrium assumption, Duprat et al. [12] have recently proposed a formulation that accounts for the effects of both the streamwise pressure gradients and the Reynolds stresses. Hence the relevant wall-function (hereafter referred to as DBMCB) is applicable in a wide range of flow conditions, including those involving boundary layer separation. In order to keep the effect of the pressure gradient, in particular, a near-wall scaling is adopted that is related to the streamwise pressure gradient through the pressure gradient velocity $u_p = |(\nu/\rho)(\partial\overline{\varpi}/\partial x_1)|^{1/3}$ [52]:

$$\widetilde{u}_1^* = \frac{\widetilde{u}_1}{u_{\tau p}}, \quad x_2^* = \frac{x_2 u_{\tau p}}{\nu}, \quad \text{with} \quad u_{\tau p} = \sqrt{u_\tau^2 + u_p^2}. \tag{15}$$

Hence, by defining the additional parameter $\alpha = u_\tau^2/u_{\tau p}^2$, and the turbulent viscosity

$$\frac{\nu_t}{\nu} = \kappa x_2^* \left[\alpha + (1-\alpha)^{\frac{3}{2}} x_2^*\right]^\beta \left[1 - \exp\left(\frac{-x_2^*}{1 + A\alpha^3}\right)\right]^2, \tag{16}$$

with $\kappa = 0.42$ the von Kármán constant, $A = 17$ and $\beta = 0.78$, the wall-function is obtained from the normalized velocity gradient

$$\frac{\partial \widetilde{u}_1^*}{\partial x_2^*} = \frac{s_{\varpi}(1-\alpha)^{\frac{3}{2}} x_2^* + s_\tau \alpha}{1 + \nu_t/\nu}, \tag{17}$$

with $s_{\varpi} = \text{sign}(\partial\overline{\varpi}/\partial x_1)$ and $s_\tau = \text{sign}(\tau_w)$. The integral of Eq. (17) between zero and the value of x_2^* measured at the sampling location gives the normalized velocity at the same location, thus providing a functional relation as in Eq. (12). The numerical integration, in particular, is performed by Gauss quadrature. Numerical tests indicate that the Gauss integration over 10 quadrature points provides sufficient accuracy for the wall-function to be valid up to about $x_2^* = 200$, whereas 20 quadrature points are enough to reach $x_2^* \simeq 1,000$.

Regarding the solution of the wall shear stress, the Ridders' iterative algorithm [46] is chosen, which provides fast convergence and robustness. It is worth noting that, after several different attempts, the most reliable solution procedure was found to be the solution of the product $\widetilde{u}_1^* x_2^* = \widetilde{u}_1 x_2/\nu$ as a function of x_2^*, given the known values of the product, which establishes whether the pressure gradient is favorable or adverse, and $u_p x_2/\nu$, which provides the minimum admissible value for the sought solution x_2^* (this follows immediately because, by the definition, $u_{\tau p}$ has to be greater than u_p). Note that the approximate procedure without iterative solution [59] triggered numerical instabilities, especially in the case of adverse pressure gradient. The tabulation technique proposed by Maheu et al. [38]

was not attempted, but remains a possible future strategy to improve the performances of the algorithm.

Finally, the heat flux at the wall, in this case, is computed following an analogous procedure as the one described by Maheu et al. [38] as

$$q_w = \frac{\mu c_p}{Pr} \left.\frac{\partial \vartheta}{\partial x_2}\right|_w = \frac{\gamma \mu x_2^*}{Pr \vartheta^* x_2}(\widetilde{e_I} - e_w), \tag{18}$$

where x_2^* is known from the solution of the velocity wall-function and the normalized temperature is obtained by Gauss integration of the normalized temperature gradient

$$\frac{\partial \vartheta^*}{\partial x_2^*} = \frac{1}{1 + (Pr/Pr_t)(\nu_t/\nu)}, \tag{19}$$

with $Pr_t = 0.85 + 2\nu/(\nu_t Pr)$ [26].

2.4 Discrete filters by Gauss quadrature integration

To obtain the filtered solution as required by the adopted LES modeling strategy, discrete filters are built using the Gauss quadrature approach described by Lodato et al. [36] (CD1 filters therein). For completeness, the relevant mathematical formulation is briefly summarized in the present section.

The use of Gauss-Legendre quadrature points allows to build a discrete filter by (approximate) analytical integration of the selected filter kernel. In particular, assuming that the convolution integral can be approximately restricted within the SD element, the 1D filtering operator can be defined as

$$\overline{\phi}(\eta) = \int_{-\infty}^{+\infty} \phi(\xi) G_\Delta(\eta - \xi) \mathrm{d}\xi \simeq \sum_{i=1}^{N} w_i^{\mathrm{G}} \phi_i G_\Delta(\eta - \xi_i), \tag{20}$$

where G_Δ is the convolution kernel associated with the low-pass filter at cutoff length Δ, and w_i^{G} are the Gaussian quadrature weights associated with the N solution points ξ_i. Choosing the Gaussian filter [49], the discrete filter weights are immediately obtained as

$$w_i^s = K w_i^{\mathrm{G}} \exp\left[-\Gamma(\beta_i^s/\alpha_s)^2\right], \tag{21}$$

where Γ is generally taken to be equal to 6, $\beta_i^s = (\xi_i - \xi_s)/\Delta$, K is a normalization coefficient and $\alpha_s \Delta$ is the desired cutoff length scale. Since the Gauss quadrature weights are strictly positive, the resulting filter weights are all positive as well, thus making this filter particularly well behaved for numerical simulations. The parameter α_s, in particular, is iteratively determined beforehand for each of the N solution points, such that the estimate of the actual cutoff length of the filter based on the second order moment of the filter kernel [37, 58] is as close as possible to the selected value of $\alpha_0 = 1.5$:

$$\frac{\alpha_0^2}{12} = \sum_{i=1}^{N} w_i^s(\alpha_s)(\beta_i^s - \xi_m)^2, \quad (s = 1, \ldots, N), \tag{22}$$

with $\xi_m = \sum_{i=1}^{N} w_i^s(\alpha_s)\beta_i^s$ (the dependance of the filter weights to the parameter α_s has been explicitly indicated for clarity). Finally, the normalization coefficient is computed such that the preservation of a constant property is satisfied, *viz.* $\sum_{i=1}^{N} w_i^s = 1$. The real part of the kernels of CD1 filters for SD elements of order 5, the same order of the computations presented in Section 3, is plotted in Fig. 3.

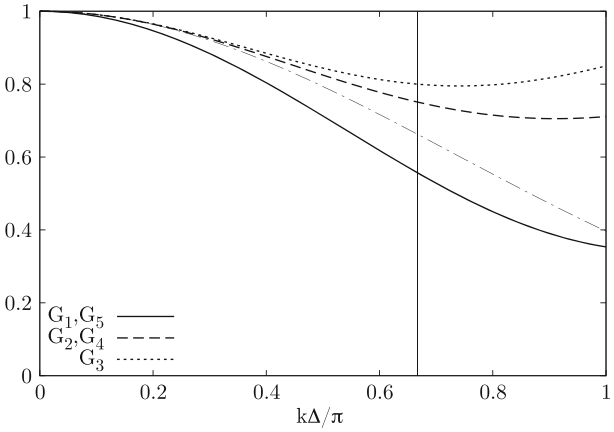

Fig. 3 Real part of the transfer function $\widehat{G}(k\Delta/\pi)$ of CD1 filters for the SD discretization of order 5 (—.—, analytical Gaussian filter)

3 Results

In the present section, results are presented from WMLES of the classical turbulent channel flow at different Reynolds numbers, and the more complex flow through a channel with periodic constrictions. It is worthwhile recalling that the purpose of the present study is not to assess the overall accuracy of the wall-models by themselves but rather to show that there exists an optimal way to integrate wall-functions and LES modeling into high-order FE type discretizations. As it will be shown in more detail in the sections that follow, both the wall-modeling strategies described in Sections 2.3.1 and 2.3.2 give accurate predictions as long as the proposed optimal approach is used.

3.1 Turbulent channel flow

Channel flow computations were performed at three different Reynolds numbers, namely, $Re_\tau = 590$, 2,000 and 4,000 (based on the friction velocity u_τ and channel half-width δ), and Mach number 0.3, and compared against the classical DNS datasets [18, 40] or reference WRLES [28, 36]. Notice that, due the extremely small density variation at $Ma = 0.3$ ($\sim$1.4 % increase from centerline to the wall), standard wall scalings are used to plot the results [14].

Grid dimensions, resolution in wall units (indicated with superscript '+') and total number of DoF are summarized in Table 1, where the last four rows refer to the wall-modeled computations. These have been performed using both the BR and DBMCB wall-functions described in Sections 2.3.1 and 2.3.2, respectively. Fourth- and fifth-order accurate computations have been carried out (i.e., $N = 4$ and 5, respectively). For reference, results from a WRLES of the $Re_\tau = 590$ test case are also included. Note that the resolution of the computation is estimated in Table 1 as the actual element size divided by the number of solution points used within the element; in a Finite Volume (FV) context, this would be equivalent to assuming that each element is filled with N^3 identical control volumes.

All the computations have been performed with periodic boundary conditions in the streamwise (i.e. along x_1) and spanwise (i.e. along x_3) directions. Isothermal walls have

Table 1 Grid size and resolution for channel flow computations

Re_τ	Label	$L_1 \times L_3$	$n_1 \times n_2 \times n_3$	N	DoF	Δ_1^+	Δ_2^+	Δ_3^+
590	CH1wr	$4\pi\delta \times \pi\delta$	$24 \times 15 \times 15$	5	6.8×10^5	62	2.3–32	25
590†	CH2wr	$2\pi\delta \times \pi\delta$	$16 \times 15 \times 8$	5	2.4×10^5	46	2.3–32	46
590*	CH3wm	$2\pi\delta \times \pi\delta$	$16 \times 8 \times 8$	5	1.3×10^5	46	20–38	46
590*	CH4wm	$2\pi\delta \times \pi\delta$	$16 \times 8 \times 8$	4	6.6×10^4	58	24–47	58
2,000*	CH5wm	$2\pi\delta \times \pi\delta$	$32 \times 16 \times 16$	5	1.0×10^6	79	18–82	79
4,000*	CH6wm	$2\pi\delta \times \frac{2}{3}\pi\delta$	$16 \times 16 \times 16$	4	2.6×10^5	393	76–163	131

(† wall-resolved computation with the same streamwise and spanwise resolution as in the wall-modeled counterpart; * wall-modeled computations)

been adopted on the top and bottom planes and modeled using Eqs. (14, 18 and 19) in the case of wall-modeled computations. In order to drive the flow, source terms s_2 and s_5 have been added to the x_1-momentum and energy equations, respectively [30, 36]. The momentum source term has been designed such as to equilibrate, at each time-step, the instantaneous resultant shear at the wall F_w, plus a relaxation term toward the expected mass flow rate $\dot{m}_0$ to accelerate convergence:

$$s_2 = \frac{F_w}{V} - \frac{\alpha}{\Delta t}(\dot{m} - \dot{m}_0), \quad \text{with} \quad \dot{m} = \frac{1}{2\delta}\int_{-\delta}^{\delta} \langle \rho u_1 \rangle \mathrm{d}x_2, \tag{23}$$

where $V = L_1 L_2 L_3$ is the volume of the computational domain, the relaxation coefficient $\alpha = 0.3$ and $\langle \cdot \rangle$ represents averaging in the streamwise and spanwise directions. The relevant work was accounted for in the energy equation as the product of s_2 and the bulk velocity [30], i.e.,

$$s_5 = u_\mathrm{b} s_2, \quad \text{with} \quad u_\mathrm{b} = \dot{m}\left[\frac{1}{2\delta}\int_{-\delta}^{\delta} \langle \rho \rangle \mathrm{d}x_2\right]^{-1}. \tag{24}$$

The computations were initialized with a uniform streamwise 4th-order velocity profile and a perturbed vertical velocity component [1, 48]. The flow was then left evolve, undergo transition to turbulence and reach the statistically steady state. After the flow field was fully developed and established, a number of statistical samples were collected in time; further ensemble averaging in the streamwise and spanwise directions was also performed. Note that, in all the results reported below, the simulation's own prediction of u_τ is used for normalization purposes.

3.1.1 Wall-resolved channel flow

Two reference WRLES have been performed at the lower Reynolds number using standard no-slip conditions at the wall. The former has been performed on a mesh (referred to as CH1wr) identical to the one used in Ref. [36], whereas for the latter (CH2wr), streamwise and spanwise grid resolutions have been set identical to those used in the WMLES. Both grids share the same vertical resolution, which is significantly higher than that adopted close to the wall for wall-modeled computations (*cf.* Table 1). Overall, the CH1wr and CH2wr meshes have between two and ten times as many DoF as the wall-modeled counterparts,

CH3wm and CH4wm. Moreover, they also share a considerably more stringent CFL limitation on the explicit time integration scheme due to the clustering of solution points close to the wall. Notice that, the grid CH1wr conforms to typical resolution requirements for WRLES [62], i.e., $\Delta_1^+ < 80$, $\Delta_3^+ < 30$ and at least three points for $\Delta_2^+ < 10$. On the contrary, although streamwise resolution is somewhat improved, the CH2wr mesh is considerably coarser in the spanwise direction (about 50 % coarser than recommended), and hence violates those guidelines.

The relevant statistics from LES on grids CH1wr and CH2wr are shown in Figs. 4 and 5, respectively, were the profiles of average streamwise velocity and root mean square (RMS) of velocity fluctuations are plotted, together with the time history of the friction coefficient, $c_f(t) = 2\tau_w(t)/(\rho u_b^2)$, normalized by the exact expected mean value (5.63×10^{-3} at $Re_\tau = 587.19$ of the DNS computation). The results from the finer mesh CH1wr are in excellent agreement with the DNS data. The measured error in the skin-friction coefficient is less than 4 %. The results computed on grid CH2wr, on the other hand, are not as good. The skin-friction coefficient is underestimated of about 14 %, which translates into the shift observed in the velocity profile within the logarithmic region. Velocity fluctuations are also over predicted close to the wall, as typically observed in the case of insufficient near-wall resolution [39].

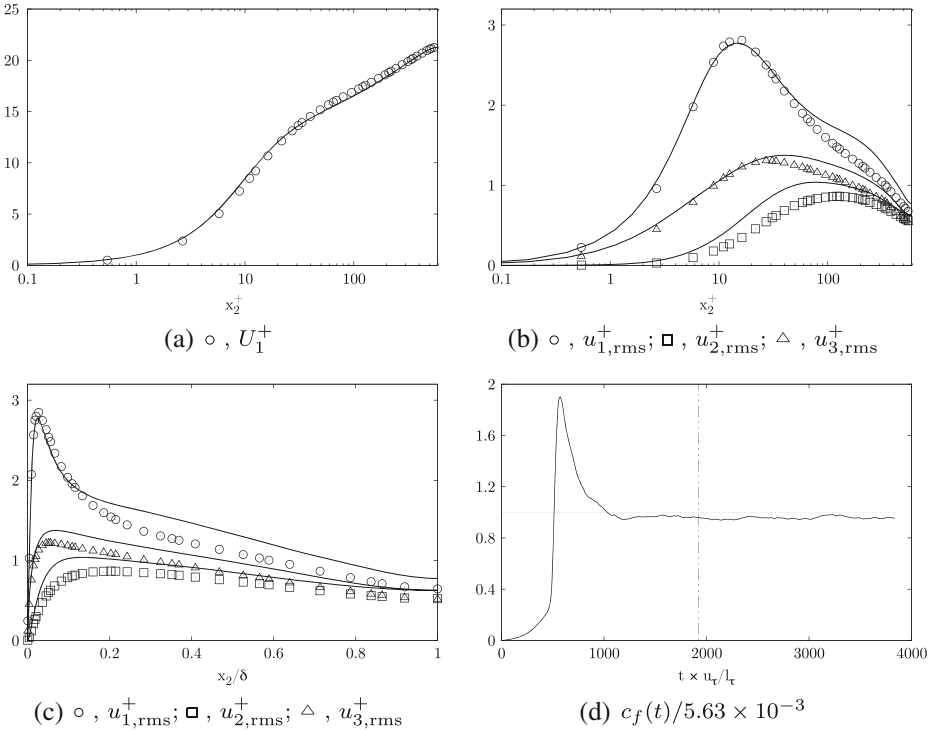

(a) ∘ , U_1^+

(b) ∘ , $u_{1,\mathrm{rms}}^+$; □ , $u_{2,\mathrm{rms}}^+$; △ , $u_{3,\mathrm{rms}}^+$

(c) ∘ , $u_{1,\mathrm{rms}}^+$; □ , $u_{2,\mathrm{rms}}^+$; △ , $u_{3,\mathrm{rms}}^+$

(d) $c_f(t)/5.63 \times 10^{-3}$

Fig. 4 WRLES on CH1wr grid with WSM model: **a** mean streamwise velocity; **b** and **c** RMS of velocity fluctuations represented with inner and outer scalings, respectively; and **d** normalized friction coefficient. DNS data [40] are represented with solid lines. *Vertical dotted line* in (d) marks the beginning of time averaging

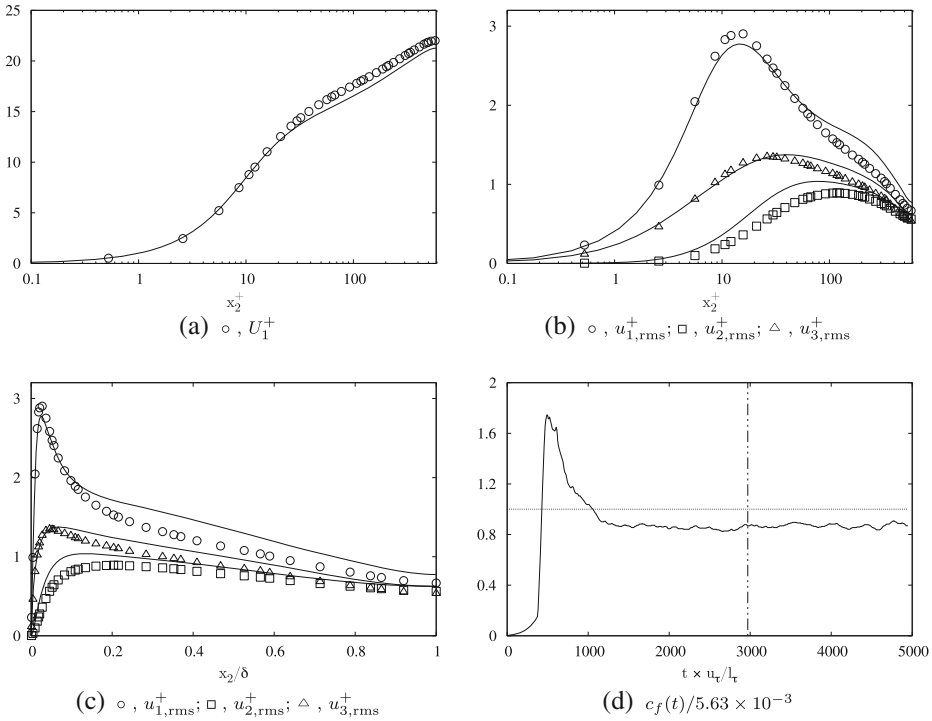

(a) ○ , U_1^+ (b) ○ , $u^+_{1,\mathrm{rms}}$; □ , $u^+_{2,\mathrm{rms}}$; △ , $u^+_{3,\mathrm{rms}}$

(c) ○ , $u^+_{1,\mathrm{rms}}$; □ , $u^+_{2,\mathrm{rms}}$; △ , $u^+_{3,\mathrm{rms}}$ (d) $c_f(t)/5.63 \times 10^{-3}$

Fig. 5 WRLES on CH2wr grid with WSM model: **a** mean streamwise velocity; **b** and **c** RMS of velocity fluctuations represented with inner and outer scalings, respectively; and **d** normalized friction coefficient. DNS data [40] are represented with solid lines. *Vertical dotted line* in (d) marks the beginning of time averaging

These reference results confirm once more that typical resolution requirements for wall-resolved LES are extremely hard to "relax", and will become useful, in the discussion that follows, to assess the overall profit in using the proposed wall-modeling technique.

3.1.2 Wall-modeled channel flow

First- and second-order statistical moments obtained from wall-modeled channel flow computations with the BR (*cf.* Section 2.3.1) and the DBMCB (*cf.* Section 2.3.2) wall-functions are plotted in Figs. 6, 7, 8 and 9. For the $Re_\tau = 590$ and 2,000, the results are compared to the available DNS data [18, 40], whereas for the $Re_\tau = 4{,}000$, the comparison is done against the results from a WRLES [28]. The extent of first wall element, having a width of about 100 wall units for $Re_\tau = 590$ and 2,000 and 300 wall units for $Re_\tau = 4{,}000$, is indicated in the plots by vertical dash-dotted lines.

Despite the simple strategy used to couple the LES region with the wall-modeled zone, the results are extremely good and encourage the use of similar zonal approaches with high-order SD methods together with a suitable SGS model, such as the WSM model adopted here. Above the modeled region, average profiles are extremely well captured. For the $Re_\tau = 2{,}000$ case, in particular, the wake region above $x_2^+ \sim 500$ is perfectly reproduced

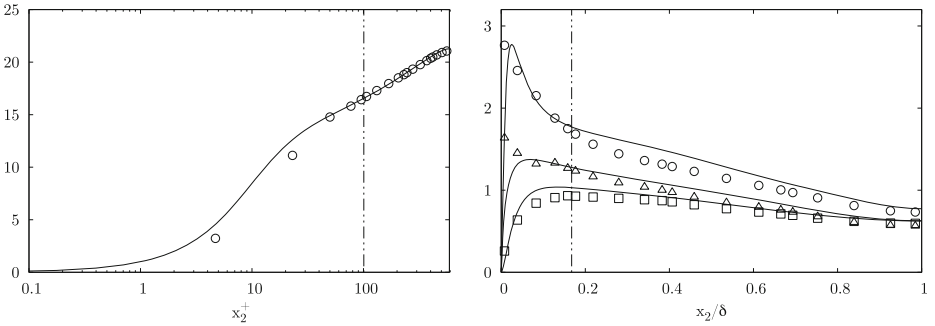

(a) BR [6], U_1^+ (b) BR [6], $u_{1,\mathrm{rms}}^+$, $u_{2,\mathrm{rms}}^+$, $u_{3,\mathrm{rms}}^+$

Fig. 6 Mean velocity profile (**a**) and RMS of velocity fluctuations (**b**) from WMLES on grid CH3wm ($Re_\tau = 590$): *open symbols*, WSM model and BR wall-function ($i_{\mathrm{lw}} = 5$); *lines*, DNS data [40]. The *vertical lines* mark the limit between wall-modeled and LES resolved regions $\left(\circ, U_1^+ \text{ or } u_{1,\mathrm{rms}}^+; \square, u_{2,\mathrm{rms}}^+; \triangle, u_{3,\mathrm{rms}}^+\right)$

(*cf.* Fig. 8a). On the other hand, the coarser mesh used at $Re_\tau = 4{,}000$ did not allow the wake region to fully develop (see Fig. 9a and c). The suppression of the wake is also observed in the WMLES results reported by Chung and Pullin [11], where the $Re_\tau = 2{,}000$ channel is

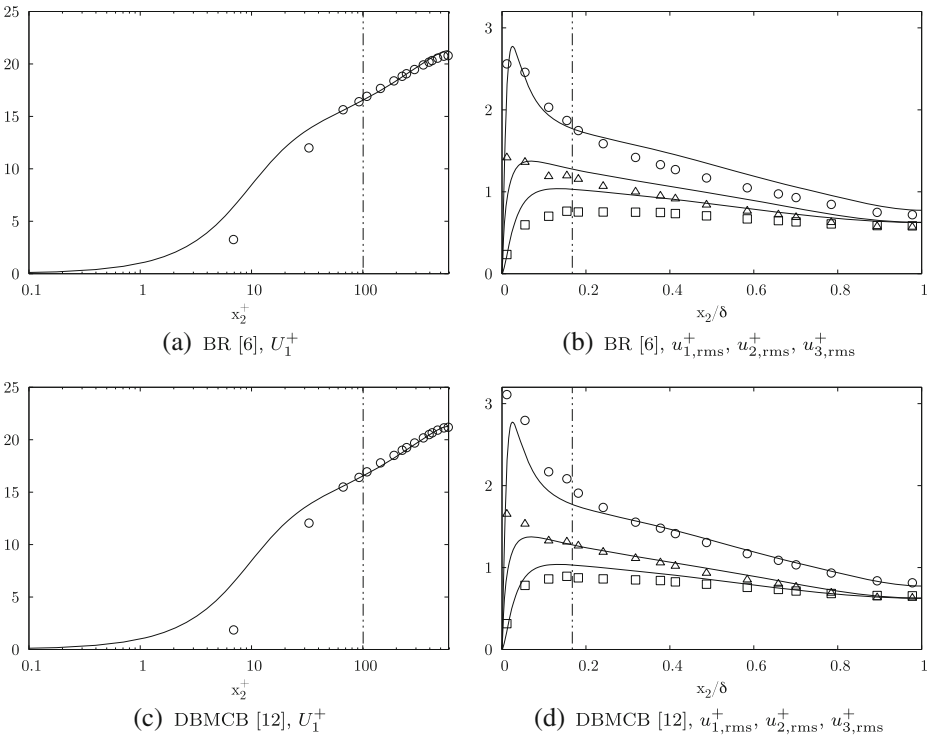

(a) BR [6], U_1^+ (b) BR [6], $u_{1,\mathrm{rms}}^+$, $u_{2,\mathrm{rms}}^+$, $u_{3,\mathrm{rms}}^+$

(c) DBMCB [12], U_1^+ (d) DBMCB [12], $u_{1,\mathrm{rms}}^+$, $u_{2,\mathrm{rms}}^+$, $u_{3,\mathrm{rms}}^+$

Fig. 7 Mean velocity profiles (**a, c**) and RMS of velocity fluctuations (**b, d**) from WMLES on grid CH4wm ($Re_\tau = 590$): *open symbols*, WSM model and BR (*top*) and DBMCB (*bottom*) wall-functions ($i_{\mathrm{lw}} = 4$); *lines*, DNS data [40]. The *vertical lines* mark the limit between wall-modeled and LES resolved regions $\left(\circ, U_1^+ \text{ or } u_{1,\mathrm{rms}}^+; \square, u_{2,\mathrm{rms}}^+; \triangle, u_{3,\mathrm{rms}}^+\right)$

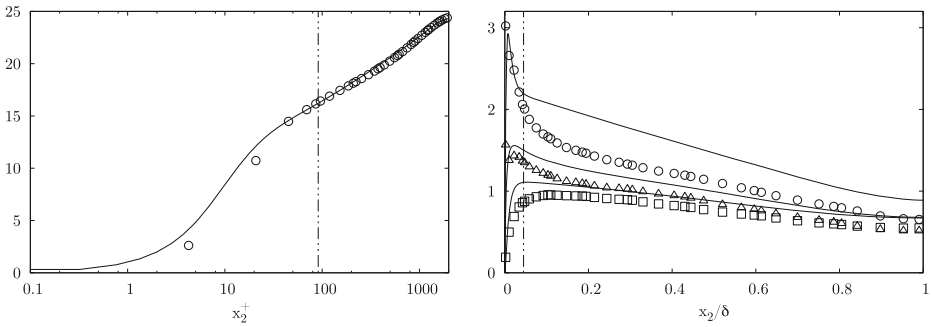

(a) BR [6], U_1^+ (b) BR [6], $u^+_{1,\mathrm{rms}}$, $u^+_{2,\mathrm{rms}}$, $u^+_{3,\mathrm{rms}}$

Fig. 8 Mean velocity profile (**a**) and RMS of velocity fluctuations (**b**) from WMLES on grid CH5wm ($Re_\tau = 2{,}000$): *open symbols*, WSM model and BR wall-function ($i_{\mathrm{lw}} = 5$); *lines*, DNS data [18]. The *vertical lines* mark the limit between wall-modeled and LES resolved regions $\left(\circ, U_1^+ \text{ or } u^+_{1,\mathrm{rms}}; \square, u^+_{2,\mathrm{rms}}; \triangle, u^+_{3,\mathrm{rms}}\right)$

computed on a mesh with $\Delta^+_{1,3} = 333$ (similar to CH6wm resolution), but not in the results by Pantano et al. [42], where the same Reynolds number was computed on a mesh with $\Delta^+_{1,3} = 87$ (similar to CH5wm resolution). Although these studies, and the present one, are characterized by different numerics and modeling approaches, the above observation seems to suggest that the mentioned wake suppression phenomenon might be due to insufficient streamwise and spanwise grid resolutions, rather than to the wall-modeling strategy.

Resolved Reynolds stresses fall generally below the DNS curves, which is expected for such relatively under-resolved grids, especially for the higher Reynolds numbers, where the SGS turbulent kinetic energy (not included in the results) represents a significant portion of the total energy. Note that the turbulent intensities for the $Re_\tau = 4{,}000$ test cases are plotted against the wall-resolved LES rather than the DNS counterparts. This explains why, in spite of the CH6wm grid being the extremely coarse, the overall degree of agreement within the outer layer seems generally better than that observed for the lower Reynolds number cases. For the more accurate fifth-order computations CH3wm and CH5wm the curves show the remarkable ability to correctly reproduce trends and peaks of velocity fluctuations even within the modeled region (i.e. $x_2^+ < 100$), especially in the streamwise and vertical directions. As expected for a classical equilibrium flow such as the turbulent channel flow, the use of either BR or DBMCB wall modeling approaches produced negligible differences with relative errors in the friction velocity of 1.3 % (BR) vs 1.5 % (DBMCB) and 2.8 % (BR) vs 1.7 % (DBMCB) for grids CH4wm and CH6wm, respectively (see Figs. 7 and 9 and Table 2).

The relative errors measured on the friction velocity are listed in Table 2 for different grids, Reynolds numbers, wall-functions and the relevant sampling locations (referred to as the i_{lw} index therein). For the higher Reynolds numbers (i.e., grids CH5wm and CH6wm), the results obtained from computations performed without any wall-function are also given to better justify the inadequacy of the relevant meshes in providing accurate WRLES results.

All the computations in which the wall-farthest sampling point was used to provide information to the wall-function reproduced a fairly accurate friction velocity, with errors that are generally smaller that 3 %. On the other hand, sampling at the first off-wall solution

point (i.e., $i_{\mathrm{lw}} = 1$) resulted in u_τ being under predicted by as much as about 40 %. Higher errors were obtained at $Re_\tau = 2{,}000$ and 4,000 when using no-slip boundary conditions without any wall model. As anticipated, the flow field at the first solution point—located in the buffer layer or around the end of the viscous sublayer (*cf.* Figs. 7, 8 and 9)—is clearly too under-resolved to provide sufficiently accurate informations to the wall-function, and definitely too far from the wall for the no-slip condition to be enforced with the right shear stress. It is worthwhile mentioning that two computations with the BR wall-function enforced at $i_{\mathrm{lw}} = 1$ became unstable when using the approximate solution approach [59]. For these computations, an iterative solution approach [46] was necessary.

As a result of the wrong friction velocity, the relevant normalized profiles (not shown) were significantly over predicted. Notice that, even though a better estimate for u_τ could be obtained by post-processing the computed mean profile through a wall-function at a higher sampling location, the relevant shear-stress would not correspond to the one applied as boundary condition during the simulation, and consequently the relevant rescaled profile would be inconsistent and characterized by the wrong slope within the logarithmic region.

To better show the negative effects of selecting the non-optimal first off-wall solution point, the profiles of velocity, this time normalized by the bulk velocity u_{b}, are plotted in Fig. 10 for the higher Reynolds numbers, where more significant errors in the friction

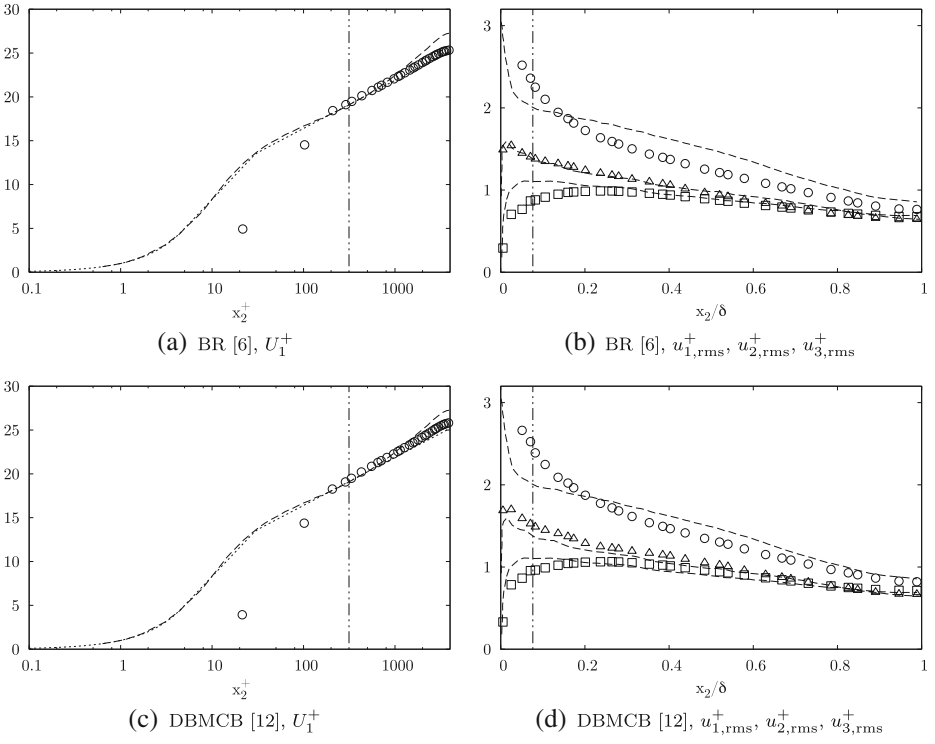

(a) BR [6], U_1^+ (b) BR [6], $u^+_{1,\mathrm{rms}}$, $u^+_{2,\mathrm{rms}}$, $u^+_{3,\mathrm{rms}}$

(c) DBMCB [12], U_1^+ (d) DBMCB [12], $u^+_{1,\mathrm{rms}}$, $u^+_{2,\mathrm{rms}}$, $u^+_{3,\mathrm{rms}}$

Fig. 9 Mean velocity profiles (**a, b**) and RMS of velocity fluctuations (**b, d**) from WMLES on grid CH6wm ($Re_\tau = 4{,}000$): *open symbols*, WSM model and BR (*top*) and DBMCB (*bottom*) wall-functions ($i_{\mathrm{lw}} = 4$); *dotted lines*, three-layers wall-function [6]; *dashed lines*, WRLES [28]. The *vertical lines* mark the limit between wall-modeled and LES resolved regions $\left(\circ, U_1^+ \text{ or } u^+_{1,\mathrm{rms}};\ \square, u^+_{2,\mathrm{rms}};\ \triangle, u^+_{3,\mathrm{rms}}\right)$

velocity were recorded for $i_{\mathrm{lw}} = 1$. For the $Re_\tau = 4{,}000$ test cases, the BR wall-function normalized by its integral is plotted for reference, i.e.,

$$f_{\mathrm{BR}}(Re_\tau y)/I_{\mathrm{BR}}, \tag{25}$$

with $f_{\mathrm{BR}}(Re_\tau y)$ from Eq. (13) and

$$I_{\mathrm{BR}} = \left[\frac{Re_\tau}{2}y^2\right]_0^{y_{\mathrm{vs}}} + \left[Ay\ln(Re_\tau y) + (B-A)y\right]_{y_{\mathrm{vs}}}^{y_{\mathrm{bf}}} + \frac{1}{\kappa}\left[y\ln(Re_\tau E y) - y\right]_{y_{\mathrm{bf}}}^{1}, \tag{26}$$

where $y = x_2/\delta$, $y_{\mathrm{vs}} = 5/Re_\tau$ and $y_{\mathrm{bf}} = 30/Re_\tau$ (other relevant constants are given in Section 2.3.1). Embedded plots with logarithmic scale are also shown to visually enhance the differences in the computed profiles within the LES resolved region. As it can be seen in the figures, the insufficient shear produced by the wall-functions when the first off-wall solution point is used causes an excessive acceleration of the flow in the vicinity of the interface of the first (modeled) element. This results in the normalized mean velocity being over predicted. As a consequence of this excess velocity and the enforcement of the nominal mass-flow rate (*cf.* Eq. (23)), the profiles become somewhat "flatter" and characterized by a noticeable deficit in the centerline velocity. Apart from the already mentioned suppression of the wake region at $Re_\tau = 4{,}000$, the profiles obtained by solving the wall-function away from the wall—i.e., 5th and 4th solution points for $Re_\tau = 2{,}000$ and 4,000, respectively—show excellent agreement with the DNS data and the reference log-law.

In order to check for the presence of unexpected numerical artifacts due to the coupling between the wall-modeled layer and the LES above it, the contours of the resolved velocity over horizontal planes located near the upmost interface of the wall element are depicted in Fig. 11. For the $Re_\tau = 590$ case, the same plane extracted from the wall-resolved LES

Table 2 Wall-modeled turbulent channel flow simulations: error in the computed friction velocity (by convention, $i_{\mathrm{lw}} = 1$ corresponds to the wall-closest solution point)

Grid	$Re_{\tau 0}$	Wall-Function	i_{lw}	Re_τ	Err. %
CH3wm	590	BR	5	602.37	2.0
		BR	1	531.39	−9.9[a]
		DBMCB	1	513.22	−13.0
CH4wm	590	BR	4	597.84	1.3
		DBMCB	4	599.04	1.5
		DBMCB	1	465.35	−21.1
CH5wm	2,000	BR	5	2,026.54	1.3
		BR	1	1,677.74	−16.1[a]
		none	–	1,653.97	−17.3
CH6wm	4,000	BR	4	4,114.44	2.8
		BR	1	2,610.16	−34.7
		DBMCB	4	4,071.28	1.7
		DBMCB	1	2,477.28	−38.0
		none	–	2,367.43	−40.8

([a] iterative solution of the wall-function was necessary)

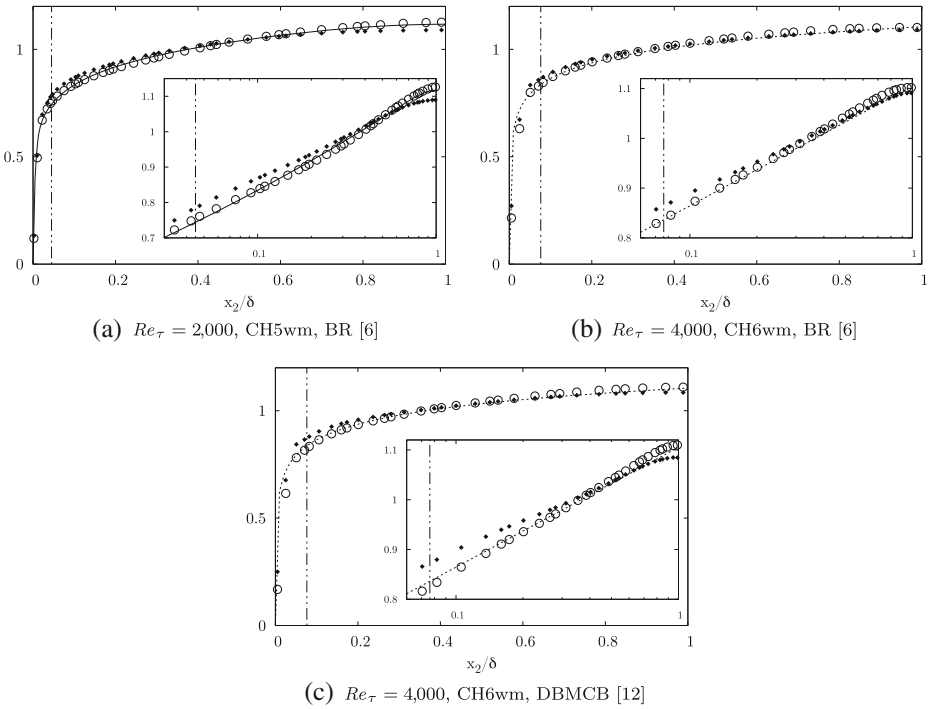

(a) $Re_\tau = 2{,}000$, CH5wm, BR [6] (b) $Re_\tau = 4{,}000$, CH6wm, BR [6]

(c) $Re_\tau = 4{,}000$, CH6wm, DBMCB [12]

Fig. 10 Streamwise mean profile normalized by the bulk velocity, $\langle u_1 \rangle / u_\mathrm{b}$: *open symbols*, WSM model and wall-functions at wall-farthest sampling point; *solid symbols*, WSM model and wall-functions at wall-closest sampling point ($i_\mathrm{lw} = 1$); *solid lines*, DNS data [18]; *dotted lines*, three-layers wall-function [6]. The *vertical lines* mark the limit between wall-modeled and LES resolved regions

(CH1wr) is also shown for reference. The visual inspection of these contours does not reveal the presence of any unphysical numerical artifact between the wall-modeled layer and the LES resolved region above it. The reference wall-resolved LES (Fig. 11a) appears smoother thanks to its higher streamwise and spanwise resolutions but, overall, the size and the shape of the turbulent structures are similar to those observed in the wall-modeled counterpart. Note that the contours for the CH6wm test in Fig. 11d are taken well within the logarithmic region ($x_2^+ = 300$), hence the (somewhat misleading) lack of fine structures compared to the $Re_\tau = 2{,}000$ case. Recalling that the LES model is not modified within the wall-modeled element (*cf.* Section 2.3), the absence of unphysical artifacts does not come with surprise. In fact, no change is made in the numerics and the model at the sampling point, whose LES solution is merely used to predict—through the wall-function—the wall shear stress that the flow has to equilibrate in a statistical sense.

3.1.3 Channel with periodic constrictions

Both wall-functions described in Section 2.3 have been tested using the same geometry adopted in other similar studies [7, 12, 55], i.e., a channel with periodic constrictions at $Re_h = 10{,}595$ (based on the bulk velocity u_b and the hill height h). A reference wall-resolved LES has been performed on a grid (referred to as PC0wr) with 72,128 elements (9.0×10^6 DoF at $N = 5$). The relevant resolution can be considered as being somewhere

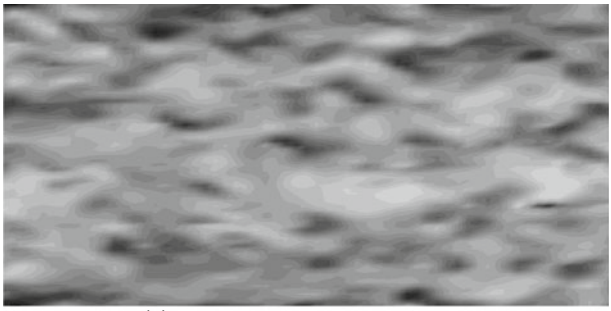

(a) $Re_\tau = 590$, wall-resolved (CH1wr)

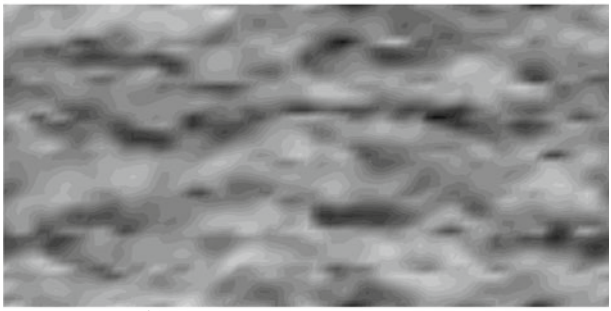

(b) $Re_\tau = 590$, wall-modeled (CH3wm)

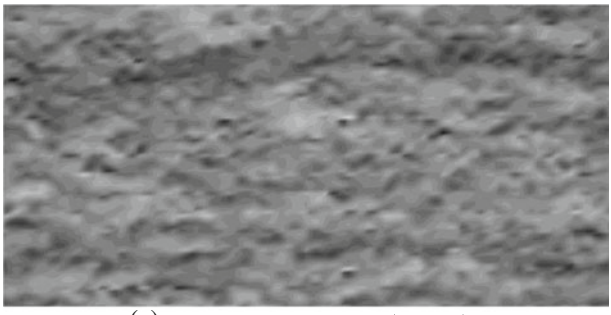

(c) $Re_\tau = 2{,}000$, wall-modeled (CH5wm)

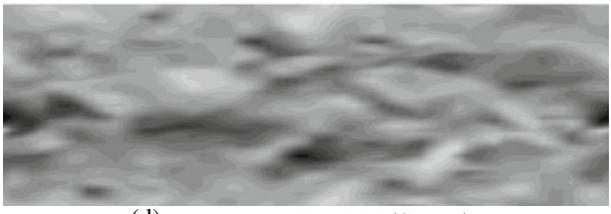

(d) $Re_\tau = 4{,}000$, wall-modeled (CH6wm)

Fig. 11 Contours of velocity magnitude at $x_2^+ = 100$ (**a, b, c**) and $x_2^+ = 300$ (**d**). Half domain length is represented in (a)

between the reference grid in Ref. [7] and grid 3 in Ref. [55]. Wall-modeled computations have been performed on a coarser mesh (PC1wm) with 5,760 elements (3.7×10^5 DoF at $N = 4$), which roughly corresponds to grid B of Ref. [12] (although this last was

characterized by a better resolution at the top wall). The two meshes are depicted in Fig. 12 and the relevant details are summarized in Table 3. Notice that the resolution of the bottom and top walls is evaluated in standard wall units measuring from the reference LES the maximum friction velocity over the hill crest and the average friction velocity over the top wall, respectively. Again, grid resolution is estimated as the element size divided by N without accounting for the actual non-uniform distribution of Gauss-Legendre quadrature points (*cf.* Fig. 1). The actual distance between the first solution point and the wall can be obtained by multiplying Δ_2^+ from Table 3 by 0.28 for the grid PC1wm, and by 0.23 for the grid PC0wr. Also note that quadratic boundary elements are used on both grids for the bottom wall to allow a more accurate prediction of the boundary layer separation point [54].

A first check is done on the profiles of the skin-friction coefficient, computed from the average shear stress as $c_f = 2\langle\tau_w\rangle/(\rho u_b^2)$, which are plotted in Fig. 13, where thick solid lines is used for the reference LES on the fine mesh.

At the bottom wall (Fig. 13a), as expected, the shear stress obtained with the no-slip boundary condition (i.e., without any wall-model) is generally underestimated in absolute

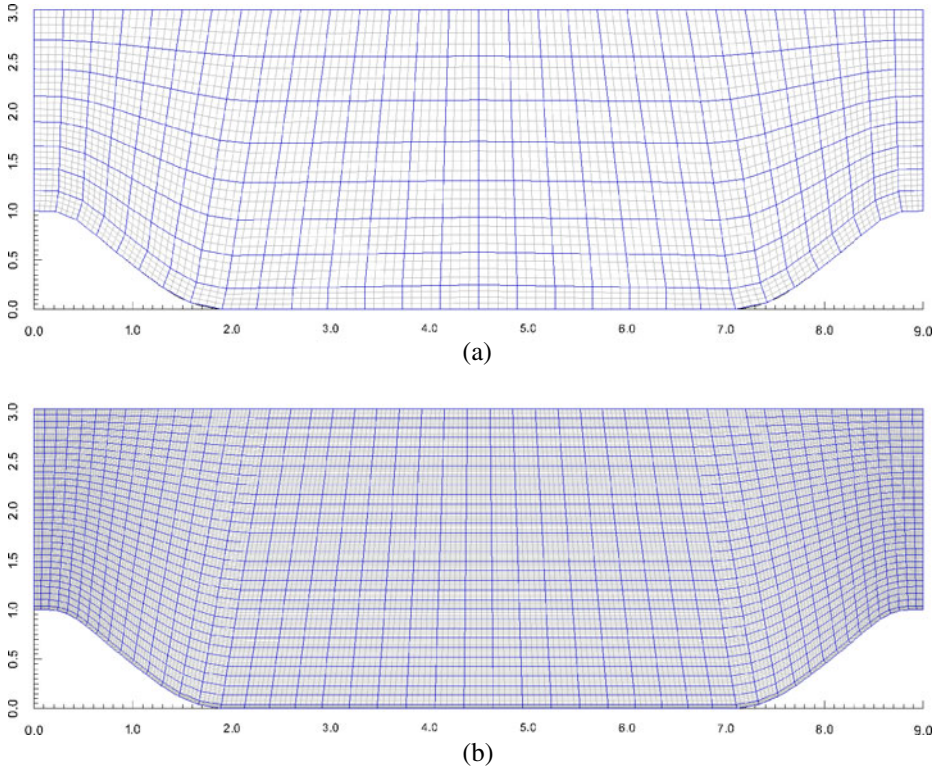

Fig. 12 Side view of the computational grids used for the channel with periodic constrictions: **a** coarse mesh for wall-modeled computations and **b** fine mesh for reference wall-resolved LES. *Blue lines* indicate the actual elements, whereas *grey lines* represent FV equivalent control volumes (*cf.* discussion about resolution in Section 3.1)

Table 3 Grid size and dimensions for computations of channel with periodic constrictions

	Label	PC0wr	PC1wm
	$n_1 \times n_2 \times n_3$	$49 \times 32 \times 46$	$30 \times 8 \times 24$
	N	5	4
	DoF	9.0×10^6	3.7×10^5
top wall	Δ_1/h	0.020–0.040	0.075
	Δ_2/h	0.014–0.020	0.078–0.120
	Δ_1^+	13–26	48
	Δ_2^+	9–13	50–77
	Δ_3^+	13	31
bottom wall	Δ_1/h	0.014–0.060	0.055–0.098
	Δ_2/h	0.008	0.050
	Δ_1^+	17–73	67–119
	Δ_2^+	10	61
	Δ_3^+	24	58
	Δ_3/h	0.020	0.048

($L_1 \times L_2 \times L_3 = 9h \times 3.035h \times 4.5h$, where h is the hill height and L_2 is the maximum distance from the top and bottom walls measured in the middle of the domain)

value. When the wall-functions are used, although negligible differences among the different computations are observed between the reattachment point ($x_1/h = 4.74$ for the reference LES) and the second separation point around $x_1/h = 7.2$, the measured skin-friction coefficient is generally improved. As expected for such a non-equilibrium boundary layer with strong pressure gradient effects, the DBMCB wall-function performs better than the BR. In particular, the best results are obtained when the sampling location is set at $i_{\mathrm{lw}} = 4$, whereas the same wall-modeling approaches applied at the wall-closest solution point deteriorate the solution. Overall, considering how coarse is the mesh used, the level

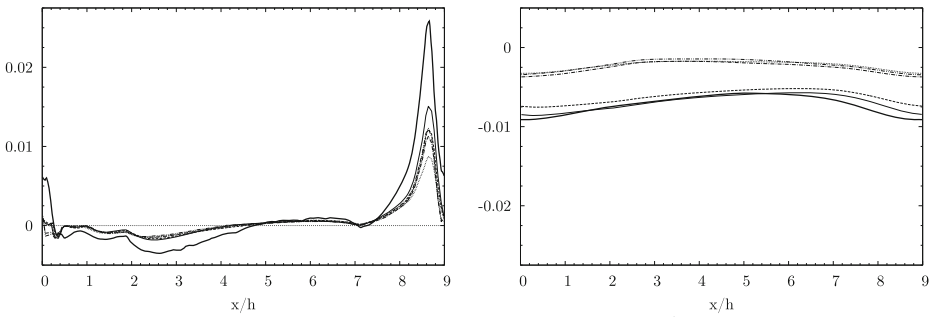

Fig. 13 Profiles of skin-friction coefficient $c_f = 2\langle\tau_w\rangle/(\rho u_{\mathrm{b}}^2)$: *thick solid line*, reference LES on grid PC0wr; *solid line*, DBMCB wall-model with $i_{\mathrm{lw}} = 4$; *dashed line*, BR wall-model with $i_{\mathrm{lw}} = 4$; *dash-dot-dotted line*, DBMCB wall-model with $i_{\mathrm{lw}} = 1$; *dash-dotted line*, BR wall-model with $i_{\mathrm{lw}} = 1$; *dotted line*, no-slip boundary condition

Table 4 Normalized separation and reattachment point locations and recirculation length

Grid	Wall-Function	i_{lw}	$(x_1/h)_{\mathrm{sep}}$	$(x_1/h)_{\mathrm{reat}}$	$(x_1/h)_{\mathrm{reat}} - (x_1/h)_{\mathrm{sep}}$
PC0wr	none	–	0.26	4.74	4.48
	none	–	0.14	4.32	4.18
	DBMCB	4	0.21	4.20	3.99
PC1wm	DBMCB	1	0.04	4.11	4.07
	BR	4	0.24	4.51	4.27
	BR	1	0.04	4.34	4.30

of agreement is very satisfactory. The location of the separation and reattachment points measured form the different computations is reported in Table 4. The computations performed with $i_{\mathrm{lw}} = 4$ give a more accurate separation location compared to those where i_{lw} is set to one or without wall-model, which determine an early separation. Similar trends in favour of setting $i_{\mathrm{lw}} = 4$ are observed for the reattachment location. Surprisingly, the BR wall-function gives a slightly better prediction of separation and reattachment.

At the top wall (*cf.* Fig. 13b), the shear stresses obtained without the wall-model or with the wall-model at the first off-wall sampling location appear significantly underestimated (in absolute value), whereas sampling away from the wall leads to the prediction of a more accurate skin-friction coefficient. This behavior is consistent with previous results from the plain channel flow computations.

For this type of flow, in general, the size and the shape of the recirculation region downstream of the hill are extremely sensitive parameters in assessing wall-modeling approaches [12]. More details about the topology of the recirculation region are given in Fig. 14, where the streamlines of the mean flow are shown for the reference WRLES on the fine mesh, and Figs. 15 and 16, where results are shown for the computations performed on the coarse meshe. Note that the shaded area in Figs. 15 and 16 corresponds to the reference WRLES on the fine mesh and serves as a reference to identify the expected length of the recirculation region.

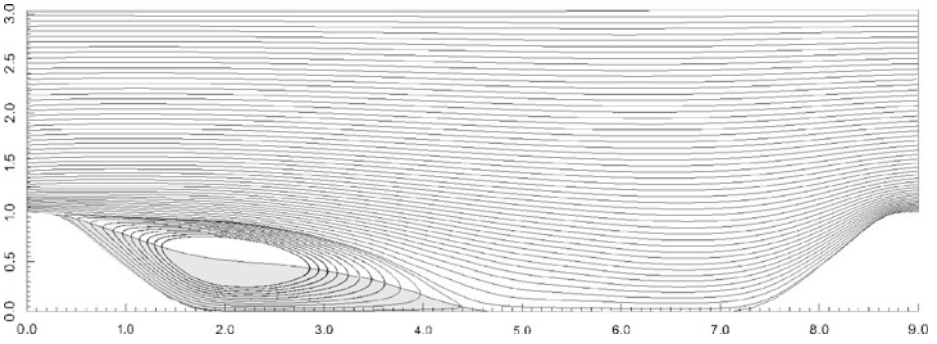

Fig. 14 Mean flow streamlines within the recirculation region for the reference LES on grid PC0wr. The shaded area represents the region of negative streamwise velocity and identifies the length of the recirculation

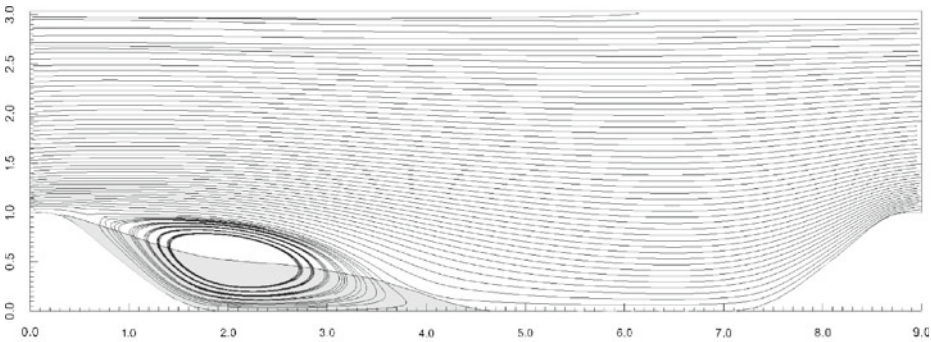

(a) DBMCB, $i_{\mathrm{lw}} = 4$

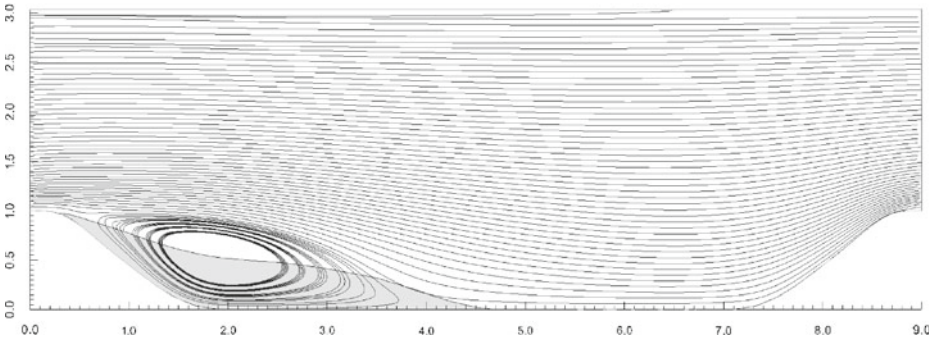

(b) DBMCB, $i_{\mathrm{lw}} = 1$

Fig. 15 Mean flow streamlines within the recirculation region: **a** DBMCB wall-model at wall-farthest sampling point; **b** DBMCB wall-model at wall-closest sampling point. The shaded area represents the region of negative streamwise velocity from the reference LES on grid PC0wr

Overall, although, as mentioned above, the wall-functions applied at the wall-farthest solution point produce a slightly more accurate separation and reattachment points, the shape of the recirculation region do not appear to be as sensitive to the particular wall treatment as it was reported by Duprat et al. [12] for an identical configuration (*cf.* Figs. 13 and 16 therein). Also notice how similar the present results on the coarse mesh PC1wm are to those computed on the finer grid A in Ref. [12], whereas the computations on grid B therein—more similar to grid PC1wm as far as resolution is concerned—show a significantly shorter recirculation region. This is most probably due to grid B therein being somewhat coarser at the bottom wall and, possibly, partly explained by the differences in the numerical approach and SGS modeling.

In Fig. 17 the profiles of mean streamwise velocity at different locations along the channel are plotted. The different computations give results which are very close to each other and which follow the reference solution reasonably well. Despite the mesh being very coarse, even the computation carried out without any wall-model, somewhat unexpectedly, provides acceptable results. Regardless of the sampling location, the use of the BR wall-function determines some relatively marginal change compared to the computation done with no-slip conditions, whereas the DBMCB wall-function determine a more significant

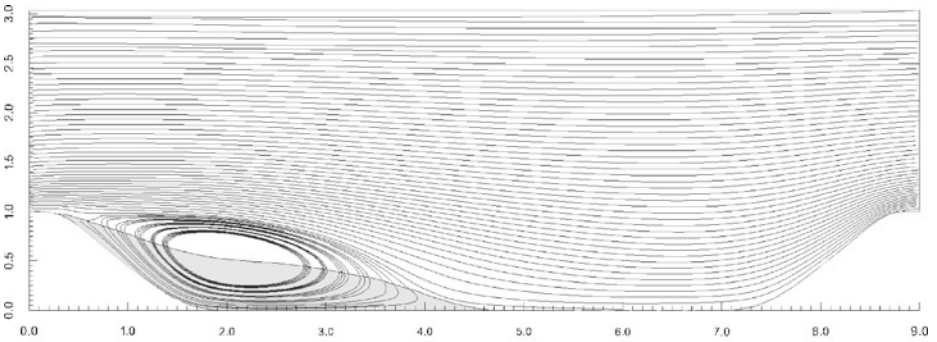

(a) BR, $i_{\mathrm{lw}} = 4$

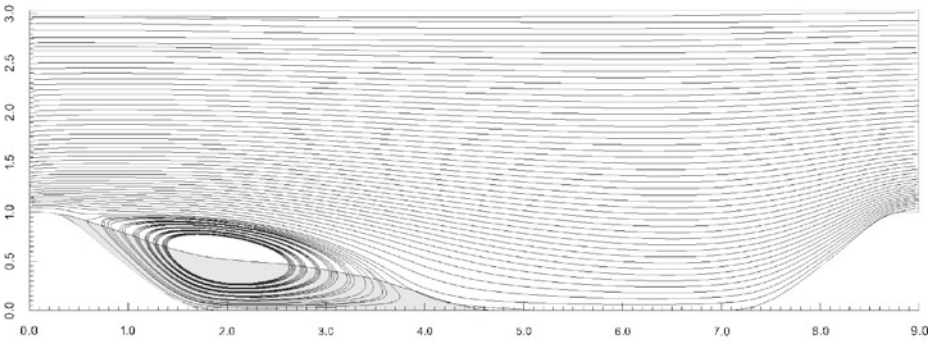

(b) BR, $i_{\mathrm{lw}} = 1$

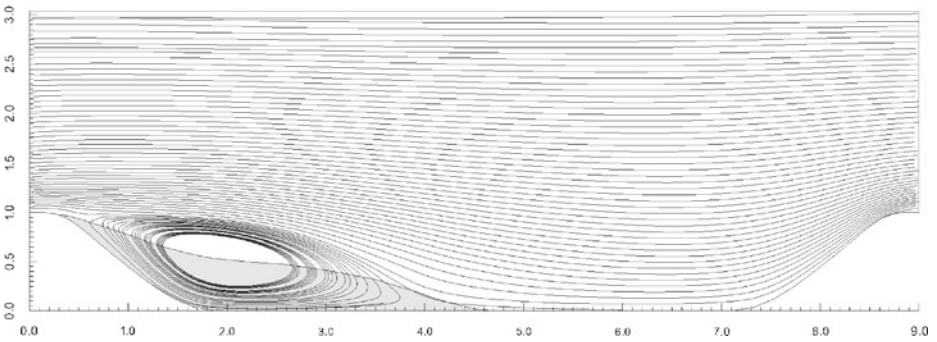

(c) no-slip condition

Fig. 16 Mean flow streamlines within the recirculation region: **a** BR wall-model at wall-farthest sampling point; **b** BR wall-model at wall-closest sampling point; **c** no-slip condition. The shaded area represents the region of negative streamwise velocity from the reference LES on grid PC0wr

improvement and, demonstrates good performances for this type of flow, especially when applied away from the wall setting $i_{\mathrm{lw}} = 4$. This further support the adoption of such strategy in conjunction with a suitable wall-modeling formulation.

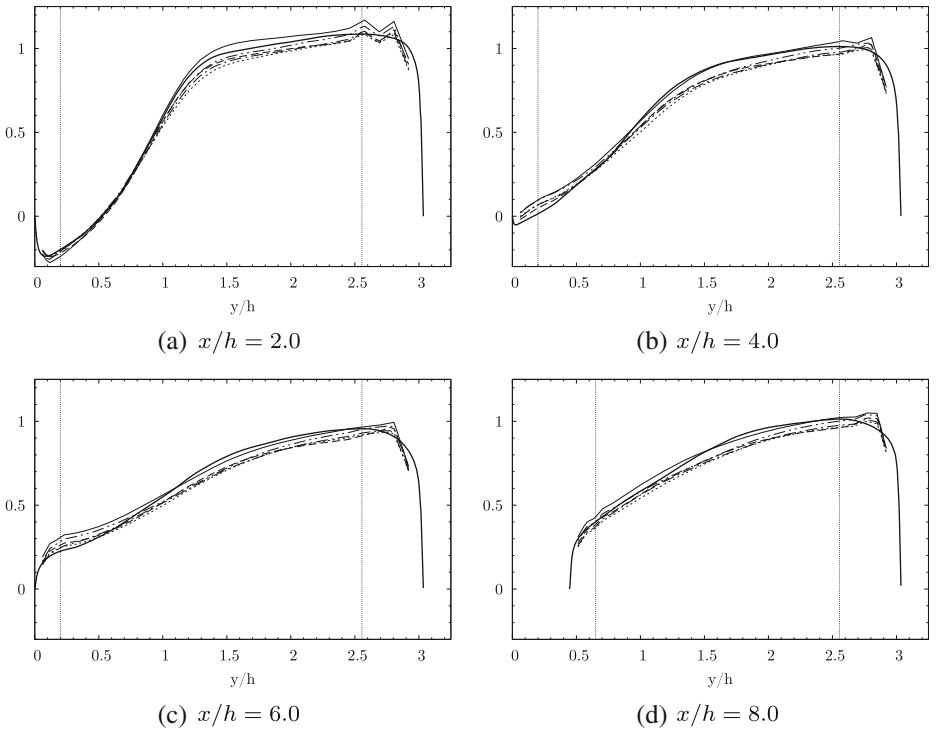

(a) $x/h = 2.0$ (b) $x/h = 4.0$

(c) $x/h = 6.0$ (d) $x/h = 8.0$

Fig. 17 Profiles of mean streamwise velocity $\langle u_1 \rangle / u_b$: *thick solid line*, reference LES on grid PC0wr; *solid line*, DBMCB wall-model with $i_{lw} = 4$; *dashed line*, BR wall-model with $i_{lw} = 4$; *dash-dot-dotted line*, DBMCB wall-model with $i_{lw} = 1$; *dash-dotted line*, BR wall-model with $i_{lw} = 1$; *dotted line*, no-slip boundary condition. The *vertical lines* mark the limit between wall-modeled and LES resolved regions

4 Concluding Remarks

An optimal strategy has been developed to couple the high-order SD method for unstructured grids, RANS type wall-functions for equilibrium and non-equilibrium turbulent boundary layers and a scale-similarity mixed model featuring dedicated discrete filters of arbitrary order. The discontinuous finite element type discretization is recognized as being an extremely well suited platform for such a hybrid RANS-LES zonal approach. Accordingly, the first element at the wall is solved such as to entirely model the viscous sub-layer and the buffer layer above, by having care to feed information to the law-of-the-wall from the better resolved solution point therein. Despite the extremely simple approach used, numerical tests on the turbulent channel flow at $Re_\tau = 590$, 2,000 and 4,000, as well as on the more complex channel with periodic constrictions at $Re_h = 10{,}595$, have proven that the proposed implementation is effective to perform accurate and reliable WMLES. For the turbulent channel flow, in particular, average velocity and turbulent intensities are extremely well captured and the measured errors in the friction velocity generally fall below 3 %, whereas applying the wall-function at the first off-wall solution point according to standard practices deteriorates significantly the results, with errors in u_τ of about 10–40 %. Moreover, the reduction in the error brought by the proposed strategy for SGS/wall-model

coupling comes essentially at no cost. The results extracted from the more challenging test case of a channel with periodic constrictions, where the boundary layer undergoes separation and reattachment, essentially confirm the benefits of the proposed strategy. Although the mean velocity profiles do not show marked differences when different approaches are used, the shape and the length of the recirculation region appear in this case better predicted when a suitable wall-function is used and applied deeper within the boundary layer.

These encouraging results, which complement ongoing efforts to develop consistent implementations of advanced LES modeling strategies in the high-order SD scheme, open the path to further exploit this numerical platform, as well as a broad range of other similar methodologies, for hybrid RANS-LES computations of complex geometries of engineering interest. Future work will be devoted to the development of more general wall-modeling strategies to perform high-fidelity LES of real systems. In particular, two extremely interesting possible additions appear to be the inclusion of a local turbulence sensor for transitional boundary layers [5] and the development of an improved approach which adapts dynamically the sampling location depending on the local resolution and the turbulence level (e.g., by varying i_{lw} from zero—meaning that no wall-model is used—to N according to the above mentioned turbulence sensor).

Acknowledgments Financial support by CNRS under the INSA Turbulence and Simulation Chair, under NSF grant No. 0915006 monitored by Dr. Leland Jameson, and AFOSR grant No. FA 9550-07-1-0195 from the Computational Math Program under the direction of Dr. Fariba Fahroo, is gratefully acknowledged. Computational resources from the Institut du Dveloppement et des Ressources en Informatique Scientifique (http://www.idris.fr) and CRIHAN (http://www.crihan.fr) are also acknowledged.

References

1. Andersson, P., Brandt, L., Bottaro, A., Henningson, D.: On the breakdown of boundary layer streaks. J. Fluid Mech. **428**(1), 29–60 (2001)
2. Balaras, E., Benocci, C., Piomelli, U.: Two-layer approximate boundary conditions for large-eddy simulations. AIAA J. **34**(6), 1111–1119 (1996)
3. Bocquet, S., Sagaut, P., Jouhaud, J.: A compressible wall model for large-eddy simulation with application to prediction of aerothermal quantities. Phys. Fluids **24**, 065,103 (2012)
4. Bodart, J., Larsson, J.: Wall-modeled large-eddy simulation in complex geometries with application to high-lift devices. In: Annual Research Briefs, Center for Turbulence Research, Stanford University, pp. 37–48 (2011)
5. Bodart, J., Larsson, J.: Sensor-based computation of transitional flows using wall-modeled large-eddy simulation. In: Annual Research Briefs, Center for Turbulence Research, Stanford University, pp. 229–240 (2012)
6. Breuer, M., Rodi, W.: Large-eddy simulation of turbulent flow through a straight square duct and a 180 bend. In: Direct and Large-Eddy Simulation I, pp. 273–285, Springer (1994)
7. Breuer, M., Kniazev, B., Abel, M.: Development of wall models for LES of separated flows using statistical evaluations. Comput. Fluids **36**(5), 817–837 (2007)
8. Cabot, W., Moin, P.: Approximate wall boundary conditions in the large-eddy simulation of high Reynolds number flow. Flow Turbul. Combust. **63**(1–4), 269–291 (2000)
9. Chapman, D.: Computatisnal aerodynamics development and outlook. AIAA J. **17**(12), 1293–1313 (1979)
10. Choi, H., Moin, P.: Grid-point requirements for large-eddy simulation: Chapmans estimates revisited. Phys. Fluids **24**, 011,702 (2012)
11. Chung, D., Pullin, D.: Large-eddy simulation and wall modelling of turbulent channel flow. J. Fluid Mech. **631**, 281–309 (2009)
12. Duprat, C., Balarac, G., Métais, O., Congedo, P., Brugière, O.: A wall-layer model for large-eddy simulations of turbulent flows with/out pressure gradient. Phys. Fluids **23**, 015,101 (2011)
13. Erlebacher, G., Hussaini, M., Speziale, C., Zang, T.: Toward the large-eddy simulation of compressible turbulent flows. J. Fluid Mech. **238**, 155–185 (1992)

14. Foysi, H., Sarkar, S., Friedrich, R.: Compressibility effects and turbulence scalings in supersonic channel flow. J. Fluid Mech. **509**(1), 207–216 (2004)
15. Harten, A.: High resolution schemes for hyperbolic conservation laws. J. Comput. Phys. **49**(3), 357–393 (1983)
16. Hesthaven, J.S., Warburton, T.: Nodal Discontinuous Galerkin Methods: Algorithms, Analysis, and Applications. Springer Science+Business Media, LLC (2008)
17. Horiuti, K.: The role of the Bardina model in large-eddy simulation of turbulent channel flow. Phys. Fluids A-Fluid **1**(2), 426–428 (1989)
18. Hoyas, S., Jiménez, J.: Scaling of the velocity fluctuations in turbulent channels up to $Re_\tau = 2003$. Phys. Fluids **18**, 011,702 (2006)
19. Huynh, H.: A flux reconstruction approach to high-order schemes including discontinuous Galerkin methods. AIAA P 2007–4079:1–42, 18th AIAA Computational Fluid Dynamics Conference, Miami, FL, Jun. 25–28, 2007 (2007)
20. Huynh, H.: A reconstruction approach to high-order schemes including discontinuous Galerkin for diffusion. AIAA P 2009–403:1–34, 47th AIAA Aerospace Sciences Meeting, Orlando, FL, Jan. 5–8, 2009 (2009)
21. Jameson, A.: A proof of the stability of the spectral difference method for all orders of accuracy. J. Sci. Comput. **45**(1), 348–358 (2010)
22. Jameson, A., Vincent, P., Castonguay, P.: On the non-linear stability of flux reconstruction schemes. J. Sci. Comput. **50**(2), 434–445 (2012)
23. Karniadakis, G., Sherwin, S.: Spectral/hp element methods for CFD. Oxford University Press, USA (1999)
24. Kawai, S., Larsson, J.: Wall-modeling in large-eddy simulation: Length scales, grid resolution, and accuracy. Phys. Fluids **24**(1), 015,105 (2012)
25. Kawai, S., Larsson, J.: Dynamic non-equilibrium wall-modeling for large eddy simulation at high Reynolds numbers. Phys. Fluids **25**(1), 015,105 (2013)
26. Kays, W.: Turbulent prandtl number, where are we? ASME Trans. J. Heat Transfer **116**, 284–295 (1994)
27. Kopriva, D., Kolias, J.: A conservative staggered-grid Chebyshev multidomain method for compressible flows. J. Comput. Phys. **125**(1), 244–261 (1996)
28. Kravchenko, A., Moin, P., Moser, R.: Zonal embedded grids for numerical simulations of wall-bounded turbulent flows. J. Comput. Phys. **127**(2), 412–423 (1996)
29. Larsson, J., Kawai, S.: Wall-modeling in large-eddy simulation: Length scales, grid resolution and accuracy. In: Annual Research Briefs, Center for Turbulence Research, Stanford University, pp. 39–46 (2010)
30. Lenormand, E., Sagaut, P., Phuoc, L.T.: Large-eddy simulation of subsonic and supersonic channel flow at moderate Reynolds number. Int. J. Numer. Meth. Fl. **32**, 369–406 (2000)
31. Lesieur, M., Métais, O., Comte, P.: Large-eddy simulations of turbulence. Cambridge University Press (2005)
32. Liang, C., Jameson, A., Wang, Z.: Spectral difference method for compressible flow on unstructured grids with mixed elements. J. Comput. Phys. **228**(8), 2847–2858 (2009)
33. Liu, S., Meneveau, C., Katz, J.: On the properties of similarity subgrid-scale models as deduced from measurements in a turbulent jet. J. Fluid Mech. **275**, 83–119 (1994)
34. Liu, Y., Vinokur, M., Wang, Z.: Spectral difference method for unstructured grids I: Basic formulation. J. Comput. Phys. **216**(2), 780–801 (2006)
35. Lodato, G., Vervisch, L., Domingo, P.: A compressible wall-adapting similarity mixed model for large-eddy simulation of the impinging round jet. Phys. Fluids **21**(3), 035,102 (2009)
36. Lodato, G., Castonguay, P., Jameson, A.: Discrete filter operators for large-eddy simulation using high-order spectral difference methods. Int. J. Numer. Meth. Fl. **72**(2), 231–258 (2013). doi:10.1002/fld.3740
37. Lund, T.: On the use of discrete filters for large-eddy simulation. In: Moin P, Reynolds W (eds) Annual Research Briefs, Center for Turbulence Research, Stanford University, pp. 83–95 (1997)
38. Maheu, N., Moureau, V., Domingo, P., Duchaine, F., Balarac, G.: Large-eddy simulations of flow and heat transfer around a low-Mach number turbine blade. In: Proceedings of the Summer Program, Center for Turbulence Research, Stanford University, pp. 137–146 (2012)
39. Meyers, J., Sagaut, P.: Is plane-channel flow a friendly case for the testing of large-eddy simulation subgrid-scale models? Phys. Fluids **19**, 048,105 (2007)
40. Moser, R., Kim, J., Mansour, N.: Direct numerical simulation of turbulent channel flow up to $\mathrm{Re}_\tau = 590$. Phys. Fluids **11**(4), 943–945 (1999)
41. Nicoud, F., Ducros, F.: Subgrid-scale stress modelling based on the square of the velocity gradient tensor. Flow Turbul. Combust. **62**(3), 183–200 (1999)

42. Pantano, C., Pullin, D., Dimotakis, P., Matheou, G.: LES approach for high Reynolds number wall-bounded flows with application to turbulent channel flow. J. Comput. Phys. **227**(21), 9271–9291 (2008)
43. Parsani, M., Ghorbaniasl, G., Lacor, C., Turkel, E.: An implicit high-order spectral difference approach for large-eddy simulation. J. Comput. Phys. **229**(14), 5373–5393 (2010)
44. Piomelli, U.: Wall-layer models for large-eddy simulations. Prog. Aerosp. Sci. **44**(6), 437–446 (2008)
45. Piomelli, U., Balaras, E.: Wall-layer models for large-eddy simulations. Annu. Rev. Fluid Mech. **34**, 349–374 (2002)
46. Ridders, C.: A new algorithm for computing a single root of a real continuous function. IEEE Trans. Circuits Syst. **26**(11), 979–980 (1979)
47. Roe, P.: Approximate Riemann solvers, parameter vectors, and difference schemes. J. Comput. Phys. **43**, 357–372 (1981)
48. Rossi, R.: Direct numerical simulation of scalar transport using unstructured finite-volume schemes. J. Comput. Phys. **228**(5), 1639–1657 (2009)
49. Sagaut, P.: Large Eddy Simulation for Incompressible Flows: An Introduction, 2nd edn. Springer-Verlag, Berlin Heidelberg (2001)
50. Salvetti, M., Banerjee, S.: *A priori* tests of a new dynamic subgrid-scale model for finite-difference large-eddy simulations. Phys. Fluids **7**(11), 2831–2847 (1995)
51. Schlichting, H., Gersten, K.: Boundary-Layer Theory, 8th edn. Springer-Verlag, Berlin Heidelberg (2000)
52. Simpson, R.: A model for the backflow mean velocity profile. AIAA J. **21**(1), 142–143 (1983)
53. Speziale, C., Erlebacher, G., Zang, T., Hussaini, M.: The subgrid-scale modeling of compressible turbulence. Phys. Fluids **31**(4), 940–942 (1988)
54. Sun, Y., Wang, Z., Liu, Y.: High-order multidomain spectral difference method for the Navier-Stokes equations on unstructured hexahedral grids. Commun. Comput. Phys. **2**(2), 310–333 (2007)
55. Temmerman, L., Leschziner, M., Mellen, C., Fröhlich, J.: Investigation of wall-function approximations and subgrid-scale models in large-eddy simulation of separated flow in a channel with streamwise periodic constrictions. Int. J. Heat Fluid. Fl. **24**(2), 157–180 (2003)
56. Vincent, P., Castonguay, P., Jameson, A.: A new class of high-order energy stable flux reconstruction schemes. J. Sci. Comput. **47**(1), 1–23 (2010)
57. Vincent, P., Castonguay, P., Jameson, A.: Insights from von Neumann analysis of high-order flux reconstruction schemes. J. Comput. Phys. **230**(22), 8134–8154 (2011)
58. Vreman, A.: The adjoint filter operator in large-eddy simulation of turbulent flow. Phys. Fluids **16**(6), 2012–2022 (2004)
59. Wang, M., Moin, P.: Dynamic wall modeling for large-eddy simulation of complex turbulent flows. Phys. Fluids **14**(7), 2043–2051 (2002)
60. Wang, Z., Fidkowski, K., Abgrall, R., Bassi, F., Caraeni, D., Cary, A., Deconinck, H., Hartmann, R., Hillewaert, K., Huynh, H., Kroll, N., May, G., Persson, P., van Leer, B., Visbal, M.: High-order cfd methods: Current status and perspective. Int. J. Numer. Meth. Fl. **72**(8), 811–845 (2013). doi:10.1002/fld.3767
61. Williams, D., Castonguay, P., Vincent, P., Jameson, A.: An extension of energy stable flux reconstruction to unsteady, non-linear, viscous problems on mixed grids. AIAA P 2011–3405:1–37, 20th AIAA Computational Fluid Dynamics Conference, Honolulu, Hawaii, Jun. 27–30, 2011 (2011)
62. Zang, T.: Numerical simulation of the dynamics of turbulent boundary layers: Perspectives of a transition simulator. Phil. Trans. R Soc. Lond. A **336**(1641), 95–102 (1991)